Model-Based Reconstruction of Spectral and Spatial Source Distribution for Objects With Known Motion

Jason M. Jaworski, *Student Member, IEEE*, Christopher G. Wahl, *Member, IEEE*, Weiyi Wang, *Member, IEEE*, Jeffrey A. Fessler, *Fellow, IEEE*, and Zhong He, *Senior Member, IEEE*

Abstract—Radiation imaging has many applications ranging from health care to homeland security and defense, and source motion is present in many of these applications. When the motion profile of the source is known or otherwise estimated, one can use motion-compensation techniques to reduce blur in the reconstructed image. In this paper, we present a model-based source-intensity reconstruction in the energy and spatial domains using list-mode data. The model includes separate parameterization for objects moving with known motion that is independent of the stationary backdrop. This approach corrects for object motion without smearing stationary sources in the backdrop space. The goal is to simultaneously obtain an estimate of the incident energy and spatial distribution of the radiation field for the stationary backdrop and for each moving object. Experimental Compton-imaging results using an 18-detector array of 3-D-position-sensitive CdZnTe detectors show that the method can successfully reconstruct the source intensity of moving objects while also revealing stationary sources in the backdrop. Also, by modeling the possibility of partial photon energy deposition in the detector, the incident energy spectrum is reconstructed more accurately.

Index Terms—Algorithms, CdZnTe, Compton imaging, image reconstruction, maximum-likelihood estimation, source motion.

I. INTRODUCTION

ACCOUNTING for motion in image reconstruction is important in many situations. In the medical field, there has been active research on this topic for many years including an early derivation of the list-mode MLEM algorithm for dynamic reconstructions by Snyder [1]. Menke *et al.* tracked patient movement by using an optical tracking system and corrected the lines of response for this motion before image reconstruction [2]. Later, Qi *et al.* expanded on the work to include the motion compensation in the reconstruction model itself [3], which, among other things, accounted for the change in sensitivity of the system as the patient moved. This improvement was an important step to reduce model mismatch.

Related work in the medical field attempts to reconstruct the time dependency of the object rather than just remove the effects of motion (e.g., 4-D poitive PET). Often, this approach uses a standard pixel mesh in the spatial domain and then uses B-splines to parameterize the time domain [4], [5]. The resulting reconstruction represents the time-dependent activity distribution, revealing physiological processes that would otherwise be unobservable with a single 3-D image. Variants of this approach have been studied, including using Fourier basis functions [6] and using list-mode data to improve temporal resolution [7] as well as many others.

In other applications, such as homeland security, imaging and/or detection of gamma-ray sources contained in moving objects is desired. For example, one can imagine placing detectors near border crossings or other choke points to detect illicit nuclear material carried in vehicles or by pedestrians. In this case, motion compensation would be required to faithfully reconstruct the intensity distributions around these (moving) objects [8]. In certain situations, there may also be stationary sources of gamma rays residing in what we refer to as the backdrop that are also of interest for imaging and detection. The work presented here focuses on this homeland security application, and assumes that the motion of the object(s) of interest are known through some other means of estimation, such as video-tracking systems [8]–[10].

The algorithm described in this paper extends the energy imaging integrated deconvolution (EIID) method of Xu and He [11]. The model developed here to account for source motion could be directly applied in detection methods that use the EIID system model, such as [12]. However, here we focus on determining the radiation distribution (in space *and* energy) originating from the moving objects, as well as from any stationary sources, while avoiding interference between them. Compton imaging using position-sensitive gamma-ray spectrometers [13]–[15], combined with a computer-controlled source-positioning system, is used to demonstrate the algorithm, though the proposed methods are general enough to accommodate other detectors and imaging modalities.

II. MODEL

A. Data Model

Let $\boldsymbol{v}$ denote an attribute vector recorded by a 3-D-position-sensitive spectrometer such as a pixelated CdZnTe detector [15]. For example, if a single incident photon results in two interactions in the detector, then $\boldsymbol{v}$ may have eight elements: the recorded energies and 3-D positions of the two interactions.

A list-mode acquisition for a fixed scan duration τ_d records n attributes $\boldsymbol{v}_1, \ldots, \boldsymbol{v}_n$ at corresponding times $t_1, \ldots, t_n$. The goal is to reconstruct the incident energy and spatial distributions from these measurements.

A gamma-ray imaging system is characterized by a system model that consists of some probability distributions that are assumed to be known, that is, are modeled based on the physics of the system. One component is the system sensitivity function

$$s(\vec{r}, E, t) = \mathsf{P}[D|\vec{r}, E, t] \tag{1}$$

which describes the probability that a gamma-ray emission from spatial position $\vec{r}$ at energy E and time t is detected (D) by the system. P is used here to denote the probability of a discrete random variable; whereas for continuous random variables we use p instead. For a single detector, $\vec{r}$ often denotes coordinates on a sphere (i.e., the far field); whereas for a system with multiple detectors, it may be reasonable to consider 3-D image reconstruction where $\vec{r} \in \mathbb{R}^3$. For simplicity, this paper focuses on the case of a single-detector system where the 2-D coordinates on a sphere are used [11]. Often when the system is stationary, the time dependence of the sensitivity is ignored [11], [16], [17], but we must include it here since our model will allow for moving objects.

In general, the sensitivity is a complicated function of the detection time t and the source energy E and position $\vec{r}$, but we describe some basic dependencies here. Since this work focuses on Compton scatter events for image reconstruction, the sensitivity is negligible below about 200 keV in CdZnTe. At about 200 keV, the sensitivity increases rapidly, peaks at about 350 keV, and then slowly decreases as the incident photon energy increases. For low-energy photons, the spatial dependence of the sensitivity is most dependent on the cross-sectional surface area of the detector as seen from the source direction. As photon energy increases, the thickness of the detector in the source direction dominates the sensitivity since high-energy photons are more likely to forward scatter.

The sensitivity becomes a function of time when the detector is in motion or when the spatial basis functions move as a function of time. This time dependence would be particularly important when reconstructing a 3-D image. In the 3-D case, any detector motion, or motion of the basis functions (as in our case), significantly changes the sensitivity of the detector system to any point in space because of the inverse square law.

Another model component that is needed is

$$f_m(\vec{r}, E, t_m) = \mathsf{p}(\boldsymbol{v}_m|\vec{r}, E, t_m, D_m)s(\vec{r}, E, t_m) \tag{2}$$

which describes the probability of recording attributes $\boldsymbol{v}_m$ for emissions of energy E originating from spatial position $\vec{r}$ for a specific event m and was derived by Wang *et al.* for our system [18]. The first term on the right describes the probability of recording $\boldsymbol{v}_m$ given that it is detected, and the second term is the sensitivity function which describes the probability of detecting the event at all. We use the time at which the event occurred t_m to correct the spatial position $\vec{r}$ for the object motion as will be described.

B. Target Object Model

For a static (stationary) scene, the usual goal is to reconstruct the radioactive source intensity distribution $\lambda(\vec{r}, E)$ in some spatial-energy domain Ω from the measured list-mode data, and the existing list-mode approach [11], [16], [19] is appropriate. This paper extends this formulation to the case where the scene consists of one or more target objects that are moving relative to a stationary backdrop, that is, the overall source intensity distribution is a function of time $\lambda(\vec{r}, E, t)$. We shall consider here the case of "known" motion, that is, the motion is estimated separately, for example, by a video-tracking system. Note that the time dependence is only present in the motion of the target through space. The intensities of the sources are assumed to be constant over the scan time in this paper.

We model the intensity distribution as consisting of an unknown stationary backdrop intensity distribution $\lambda_0(\vec{r}, E)$ and a set of K target objects that may be moving. The unknown intensity distribution of the kth object at time $t = 0$ is denoted

$$\lambda_k(\vec{r}, E) = \lambda_k(\vec{r}, E, 0) \tag{3}$$

for $k = 1 \ldots K$. For simplicity of presentation, we assume that the target-object motion can be modeled adequately by spatial translation. Other forms of motion, such as rotation, could be accommodated as well. The spatial shift of the kth target object at time t is denoted $\vec{c}_k(t)$, where $\vec{c} \in \mathbb{R}^3$ for a 3-D imaging problem or $\vec{c} \in \mathbb{R}^2$ for the 2-D case. Under this assumption, we model the intensity distribution of the kth target object at time t as

$$\lambda_k(\vec{r}, E, t) = \lambda_k(\vec{r} - \vec{c}_k(t), E). \tag{4}$$

Also for simplicity, our model ignores occlusions and the absorption of gamma photons by target objects that move in front of one another.

Finally, we model the overall time-varying intensity distribution of the scene as the superposition of the stationary backdrop $\lambda_0(\vec{r}, E)$ and the moving target-object contributions

$$\begin{aligned} \lambda(\vec{r}, E, t) &= \lambda_0(\vec{r}, E) + \sum_{k=1}^{K} \lambda_k(\vec{r}, E, t) \\ &= \lambda_0(\vec{r}, E) + \sum_{k=1}^{K} \lambda_k(\vec{r} - \vec{c}_k(t), E). \end{aligned} \tag{5}$$

The goal is to reconstruct the intensity distributions of the backdrop and the target objects, i.e., $\{\lambda_0(\vec{r}, E), \lambda_1(\vec{r}, E), \ldots, \lambda_K(\vec{r}, E)\}$, from the list-mode data, assuming known motion $\vec{c}_k(t)$ for $k = 1, \ldots, K$.

To facilitate numerical implementation, the intensity distributions are parameterized using a finite-series model [20]

$$\lambda_0(\vec{r}, E) = \sum_{j=1}^{N_0} \lambda_{0j} b_{0j}(\vec{r}, E) \tag{6}$$

where N_0 is the total number of basis functions in the backdrop, λ_{0j} denotes the unknown intensity of the jth basis function, and b_{0j} denotes the basis function (typically a 2-D region of space in spherical coordinates or a 3-D "voxel" in Cartesian coordinates,
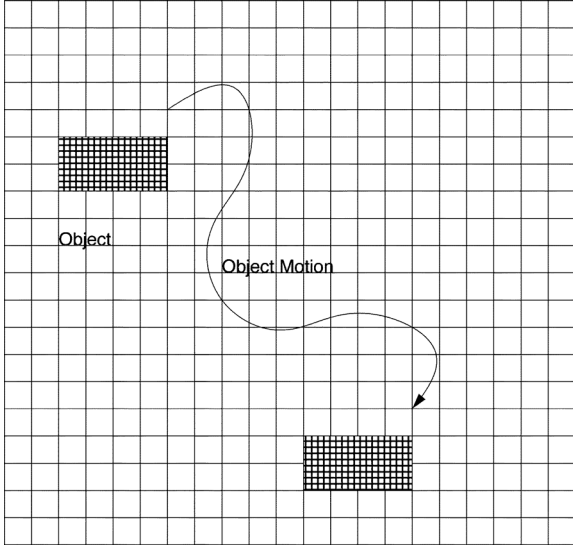
Fig. 1. Illustration of target-object model with a pixelated stationary backdrop and one pixelated target object that moves during the imaging process.

covering an energy interval). The basis functions are non-negative, which ensures that the estimate is also non-negative. Convergence of the MLEM algorithm that will be described also uses this non-negativity assumption [21]. Similarly, we parameterize the moving target objects (at time $t = 0$) as

$$\lambda_k(\vec{r}, E) = \sum_{j=1}^{N_k} \lambda_{kj} b_{kj}(\vec{r}, E) \qquad (7)$$

where the number of basis functions N_k used to represent the kth target object may differ between target objects of different sizes. If the kth moving target object is treated as a point source, then N_k reduces to the number of energy bins. The overall time-varying intensity distribution is thus parameterized as

$$\lambda(\vec{r}, E, t) = \sum_{k=0}^{K} \sum_{j=1}^{N_k} \lambda_{kj} b_{kj}(\vec{r} - \vec{c}_k(t), E) \qquad (8)$$

where the backdrop mesh has been included over the target sum for conciseness and $\vec{c}_0(t) \equiv 0$. Typically, the basis functions are unitless and the coefficients λ_{kj} have units of "emissions per unit time per unit solid angle (or volume) per unit energy."

With this parameterization, the goal is to estimate the coefficients of the backdrop $\{\lambda_{0j}\}$ and of the targets $\{\lambda_{kj}, k = 1, \dots, K\}$ from the list-mode data.

Fig. 1 illustrates the model. Note that if the kth target object does not move, then this formulation could be over-parameterized because the intensity within the support of that target object could be modeled by the target-object pixel λ_{kj} and a corresponding backdrop pixel $\lambda_{0j'}$, in the case that $b_{kj}(\vec{r})$ and $b_{0j'}(\vec{r})$ overlap. Therefore, one should include only moving target objects in this formulation; otherwise, the solution will not be unique. (Stationary sources will be reconstructed as part of the backdrop.)

III. ALGORITHM

The Appendix shows that the list-mode log likelihood for a time-varying emission distribution $\lambda(\vec{r}, E, t)$ is

$$\sum_{m=1}^{n} \log \left(\iint_{\Omega} f_m(\vec{r}, E, t_m)\lambda(\vec{r}, E, t_m)\mathrm{d}\vec{r}\,\mathrm{d}E \right) - \bar{M}_\lambda \quad (9)$$

where the expected number of recorded counts during a measurement time of τ_d is given by

$$\bar{M}_\lambda = \int_0^{\tau_d} \iint_{\Omega} s(\vec{r}, E, t)\lambda(\vec{r}, E, t)\mathrm{d}\vec{r}\,\mathrm{d}E\,\mathrm{d}t. \quad (10)$$

Substituting in the finite-series model (8) yields a list-mode log-likelihood expression in terms of the coefficients $\{\lambda_{0j}\}$ and $\{\lambda_{kj}\}$. After some algebraic manipulation, the log likelihood is simplified to the following form:

$$\sum_{m=1}^{n} \log \left[\sum_{k=0}^{K} \sum_{j=1}^{N_k} \lambda_{kj} f_{kjm} \right] - \sum_{k=0}^{K} \sum_{j=1}^{N_k} \lambda_{kj} g_{kj} \quad (11)$$

where we define

$$f_{kjm} = \iint_{\Omega} \mathsf{p}(\boldsymbol{v}_m | \vec{r}, E, t_m, D_m) s(\vec{r}, E, t_m)$$
$$\cdot\, b_{kj}(\vec{r} - \vec{c}_k(t_m), E)\,\mathrm{d}\vec{r}\,\mathrm{d}E, \quad (12)$$

$$g_{kj} = \int_0^{\tau} \iint_{\Omega} s(\vec{r}, E, t)b_{kj}(\vec{r} - \vec{c}_k(t), E)\,\mathrm{d}\vec{r}\,\mathrm{d}E\,\mathrm{d}t. \quad (13)$$

Here, g_{kj} describes the overall sensitivity of the detector to emissions from the jth spatial-energy voxel of the kth target and f_{kjm} describes the probability of recording event i given that it came from the jth spatial-energy voxel of the kth target.

The likelihood function (11) is of a form where it is appropriate to use the standard MLEM algorithm derived by Parra and Barrett [19], yielding the following update equation:

$$\lambda_{kj}^{i+1} = \frac{\lambda_{kj}^i}{g_{kj}} \sum_{m=1}^{n} \frac{f_{kjm}}{\sum_{k'=0}^{K} \sum_{j'=1}^{N_{k'}} \lambda_{k'j'}^i f_{k'j'm}}. \quad (14)$$

The key term of this more general form of the MLEM algorithm is the time integral of the system sensitivity in (13). Due to motion of the object and/or the system itself, we compute (13) by Riemann sum over a list of discretized target and detector positions and rotations. An example where this generalization is important is when a target gets very close to the system during the measurement time. If relatively few counts are recorded during that period, the instantaneous sensitivity $s(\vec{r}, E, t)$ would be large for only a small fraction of events, but the integrated sensitivity g_{kj} would be large and that high overall sensitivity would suppress the reconstruction from estimating a source that passes that direction.

IV. EXPERIMENTS

A. Detector Array System

The detector array system used in this paper consists of 18 $2.0 \times 2.0 \times 1.5$-cm 3-D-position-sensitive room-temperature-pixelated CdZnTe detectors. The array operates as a single detector, that is, if a photon scatters from one detector module into another, the system reads that as one event and is able to use it for Compton imaging. The system is able to achieve 1.08% single-pixel and 1.44% overall FWHM energy resolution at 662 keV. By recording which anode pixel(s) collected the electrons generated by the photon interaction(s), the 2-D-lateral position(s) are known within the pixel pitch of 1.72 mm. The depth of interaction is determined by either the cathode-to-anode signal ratio for single-pixel events or drift time for multiple-pixel events, with a resolution of about 1 mm [22], [23]. The energy and 3-D position of each interaction for each event (incident photon) are recorded in list mode. These list-mode data for 2-, 3-, and 4-pixel events constitute the attribute vectors $\boldsymbol{v}_m$ used for image reconstruction.

Wang et al. [18] describe the system model $f_m(\vec{r}, E, t_m)$ that we use for pixelated CdZnTe detectors in detail. In brief, the model accounts for several physical phenomena, including attenuation, scattering, and absorption of the incident photons. The attenuation probabilities are calculated for the photons as they travel through the active detector volume only (i.e., ignoring attenuation through the electronics or enclosure materials). The model also includes the probability that a particular photon interaction is a Compton scatter or photoelectric absorption as well as the probability that the photon eventually escaped the detector (i.e., the full energy of the photon was not recorded).

Xu [24, p. 130] describes in detail how we calculate the sensitivity of the system $s(\vec{r}, E, t = 0)$ by using a single iteration of the standard MLEM algorithm with data from a simulated source uniform in space and energy. Using this sensitivity and system model in the stationary case, the standard MLEM algorithm estimates the photon emission distribution in energy and space. In this paper, we assume the sources are in the far field. Therefore, we model the source distribution as the surface of a sphere rather than as 3-D distribution.

B. Source Motion

To demonstrate the presented algorithm experimentally, a method of recording the source position as a function of time was required. Thus, we assembled the apparatus shown in Fig. 2 to rotate a source around the 18-detector array. A computer-controlled actuator, attached to the top of a table, was set to rotate with a constant angular velocity to known angular displacements. An "L"-shaped aluminum arm was attached to this actuator so that the bottom-most tip of the arm was in the plane of the array system positioned below the table. Then, we placed the center of the detector head directly below the actuator pivot point so that the resulting motion at the bottom-most tip of the actuator arm would revolve completely around the center of the detector array.
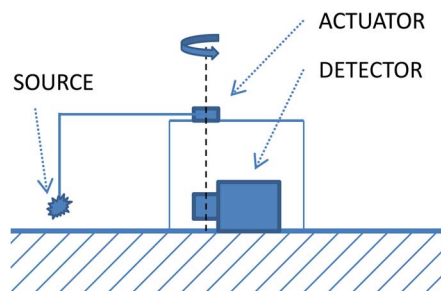
Fig. 2. Computer-controlled actuator arm, which is mounted to a table, is used to control the position of the source with known motion. The detector system is depicted as two rectangles. The smaller rectangle contains the actual CdZnTe crystals, and the larger body contains the supporting electronics, including high- and low-voltage power supplies and the data readout. The array of detectors is positioned directly underneath the actuator pivot point, and the source is placed at the bottom of the actuator arm, inplane with the detectors.
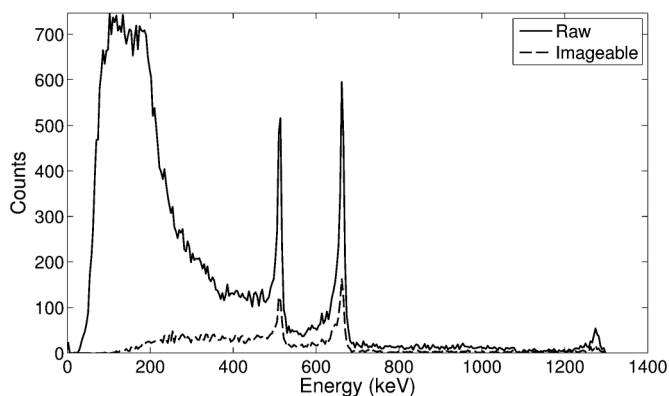
Fig. 3. Raw and imagable energy spectra of the events used for the image reconstruction of a moving ^{137}Cs source and stationary ^{22}Na source described in Section V-A.

V. RESULTS

A. One Moving and One Stationary Source

In the first experiment, a 122-μCi ^{137}Cs source was rotated 360° at a constant angular velocity around the detector system at a radius of 1.2 m during the course of a 46-min measurement in the counterclockwise direction (when viewed from the top). Also, a ^{22}Na source was placed in a stationary position in the backdrop 1.0 m from the center of the detector. Because of computational constraints, a smaller set of events was used for the following reconstructions. To use data from the entire data-collection time, the first event of every 50 events was used for each reconstruction of this data set, which resulted in 3928 imagable events in the energy range of 300 to 1300 keV. An imagable event is defined as a recorded 2-, 3-, or 4-pixel event. The energy spectrum of imagable events is shown in Fig. 3 along with the overall raw spectrum which includes all recorded counts.

1) Standard MLEM Reconstruction: A standard list-mode MLEM reconstruction, which reconstructs only the spatial domain, is performed to be compared with the new algorithm presented in this paper. No motion compensation is performed, and energy windows are used so that only photopeak counts are reconstructed.

Figs. 4 and 5 show the reconstructed images of the standard MLEM reconstruction after 20 EM iterations using a 36
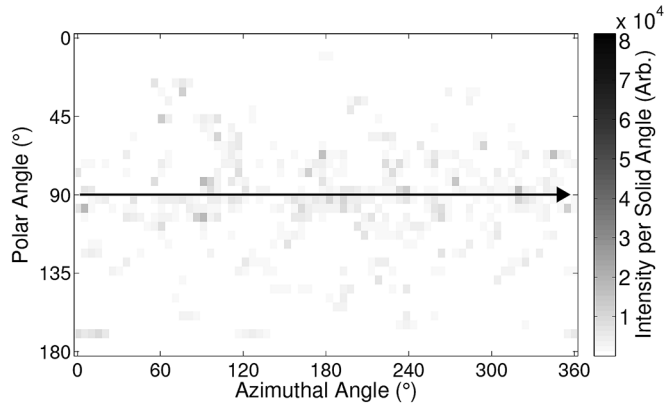
Fig. 4. Results for the standard MLEM spatial reconstruction for the ^{137}Cs energy window (620–700 keV). The estimated intensity is smeared through the equator since no motion compensation was applied and the source was in constant motion. The motion path is described by the arrow in the image.
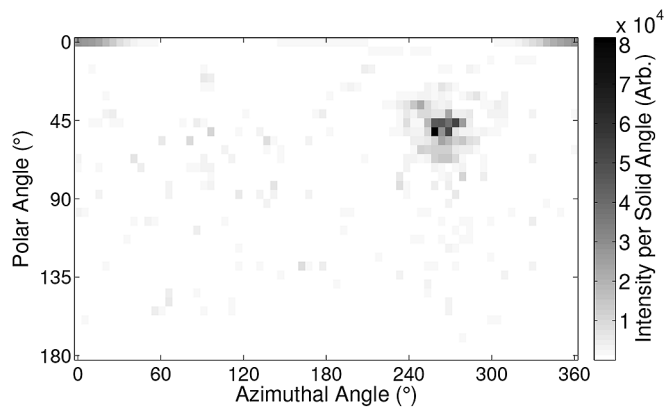
Fig. 5. Results for the standard MLEM spatial reconstruction for the ^{22}Na energy window (490–530 keV and 1100–1200 keV). A single localized hotspot is visible, corresponding to the location of the stationary ^{22}Na source.

$\times$ 72 pixel backdrop imaging mesh (over 4π). Fig. 5 shows that the spatial distribution for the ^{22}Na photopeak energy range is deconvolved correctly as expected since the source was stationary. However, the deconvolved spatial distribution for the ^{137}Cs photopeak window, seen in Fig. 4, does not show a clear hotspot since the source was in constant motion, and that motion was not included in the model.

2) MLEM Reconstruction Using Separate Target Binning: The same data are reconstructed using the newly proposed method with a similar backdrop mesh and a 9×9 pixel target-object mesh spanning $40°$ in the polar and azimuthal directions. We use 250 evenly spaced energy bins over a range of 300–1300 keV since relatively few imagable events fall outside this energy range, and the accuracy of the system model degrades below 300 keV. Thus, we limit the energy dimension to this set of energies.

Figs. 6–8 show the reconstructed images after 20 EM iterations of the proposed model-based algorithm. The desired results in this situation would estimate a single hotspot in the stationary backdrop with a ^{22}Na spectrum and a hotspot at 662 keV in the target object space, which tracked the ^{137}Cs source motion. The actual reconstruction for the backdrop space, seen in Fig. 6, is similar to the desired result. Fig. 6(b) shows the single
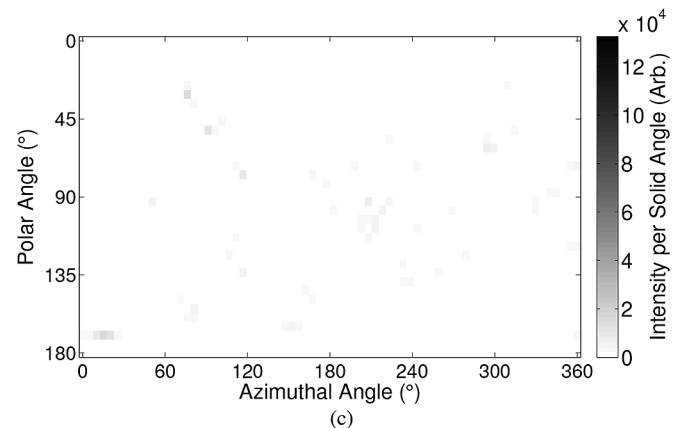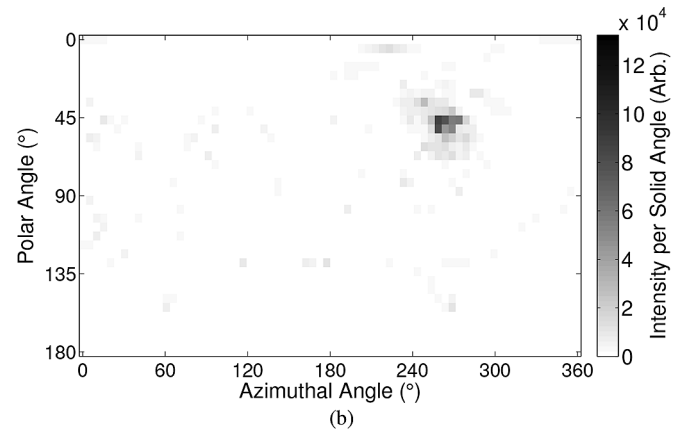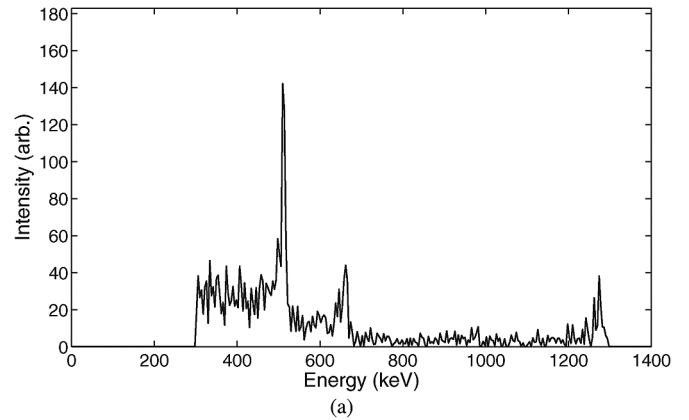
Fig. 6. Results for the backdrop space after 20 iterations of the proposed motion-compensated EM algorithm for a moving ^{137}Cs source and a stationary ^{22}Na source: (a) reconstructed incident energy spectrum for the entire backdrop space, (b) reconstructed spatial distribution for the ^{22}Na energy window (490–530 keV and 1100–1200 keV), and (c) reconstructed spatial distribution for the ^{137}Cs energy window (620–700 keV).

hotspot at the ^{22}Na energies, and even though there is again some ^{137}Cs contamination in the backdrop seen in Fig. 6(c), it still does not form a single hotspot but is distributed over the entire 4π space.

Fig. 6(a) shows the reconstructed spectrum for the entire backdrop space, but it has a significant amount of ^{137}Cs contamination. Fig. 7 shows the spectrum just in the direction of the stationary ^{22}Na source, which is a well-deconvolved ^{22}Na spectrum as expected. Fig. 8 shows the reconstruction results for the target object space. The reconstructed spectrum shown
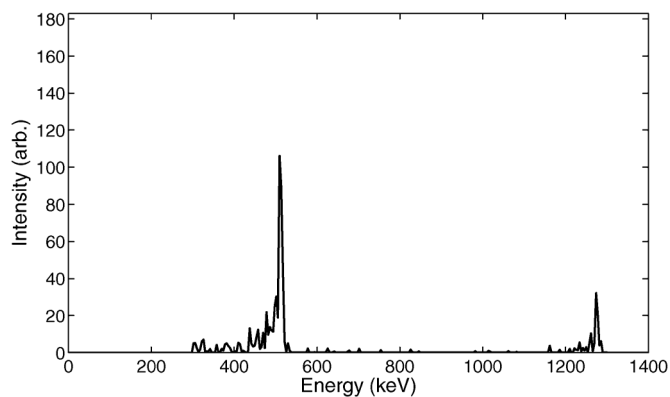
Fig. 7. Reconstructed incident energy spectrum corresponding to just the hotspot direction in Fig. 6(b).
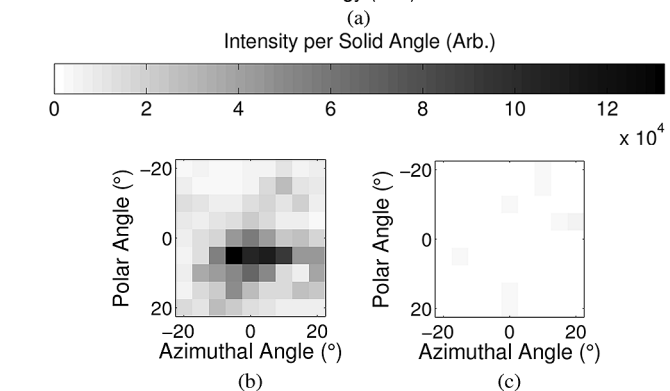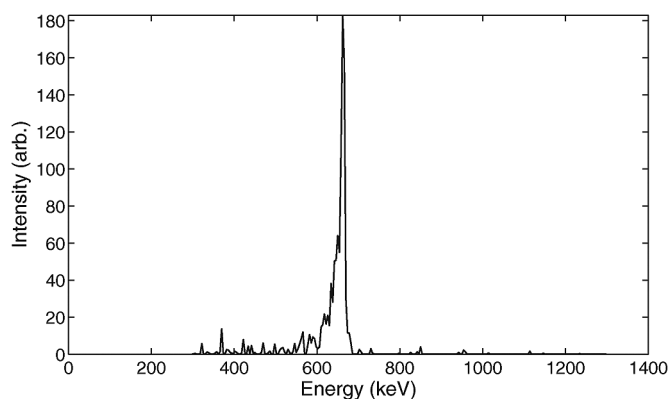
Fig. 8. Results for the target-object space after 20 iterations of the proposed motion-compensated EM algorithm for a moving ^{137}Cs source and a stationary ^{22}Na source: (a) reconstructed incident energy spectrum for this target, (b) reconstructed spatial distribution for the ^{137}Cs energy window (620–700 keV), and (c) reconstructed spatial distribution for the ^{22}Na energy window (490–530 keV and 1100–1200 keV).

in Fig. 8(a) is a well-deconvolved ^{137}Cs spectrum free of ^{22}Na contamination. Fig. 8(b) shows the hotspot at the ^{137}Cs energy, and Fig. 8(c) shows that there is no crosstalk at the ^{22}Na energies.

For comparison of the reconstruction quality with the simplest case of a single stationary source and no target bins, we performed an experiment to reconstruct the image of a single stationary ^{22}Na source using a similar number of counts from the source as in the preceding experiment and the same number of iterations. The resulting image looks very similar to Fig. 6(b),
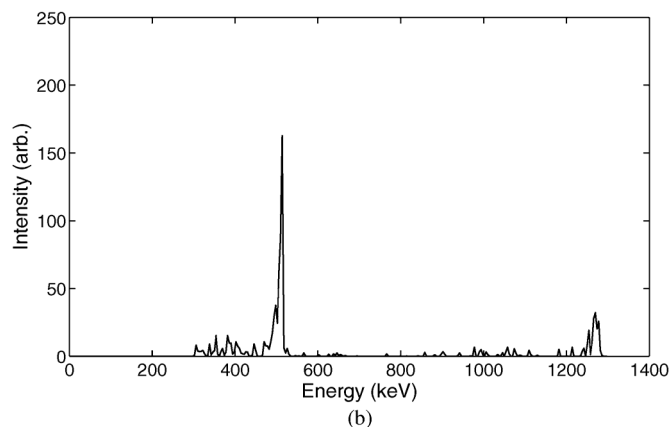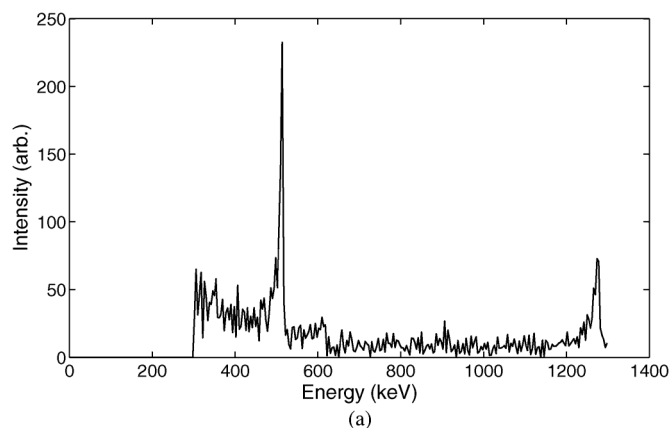
Fig. 9. The reconstructed incident energy spectrum, after 20 iterations, for a single stationary ^{22}Na source (a) integrated over all space and (b) corresponding to just the source direction.

and the resulting spectra for all directions and just the source direction are shown in Fig. 9. Compare these spectra with those in Figs. 6(a) and 7. Although the ^{137}Cs source does have an effect on the overall backdrop spectrum, the reconstructed directional spectrum is essentially independent of the presence of the moving ^{137}Cs source.

B. Two Sources Moving in Opposite Directions

In the second motion experiment, the same ^{137}Cs source was rotated 360° around the detector system similar to the first experiment, and then the previously stationary ^{22}Na source was rotated 360° around the detector in the opposite direction in a similar fashion. The two datasets were then combined and reconstructed as if they occurred simultaneously with the sources, crossing paths at 180° in the azimuthal direction. This combined dataset, consisting of 4449 imagable events in a similar energy range (after downsampling), was reconstructed using similar imaging and energy meshes as the previous experiment (except that now there are two target-object meshes tracking the two moving sources). The standard nonmotion-compensated MLEM image for this dataset looks very similar to that of the ^{137}Cs energy window in the first reconstruction: a smear of intensity through the equator, and without tracking information, the two sources would appear to simply overlap. The raw spectrum for the events used in this reconstruction is similar to that of the first reconstruction seen in Fig. 3.
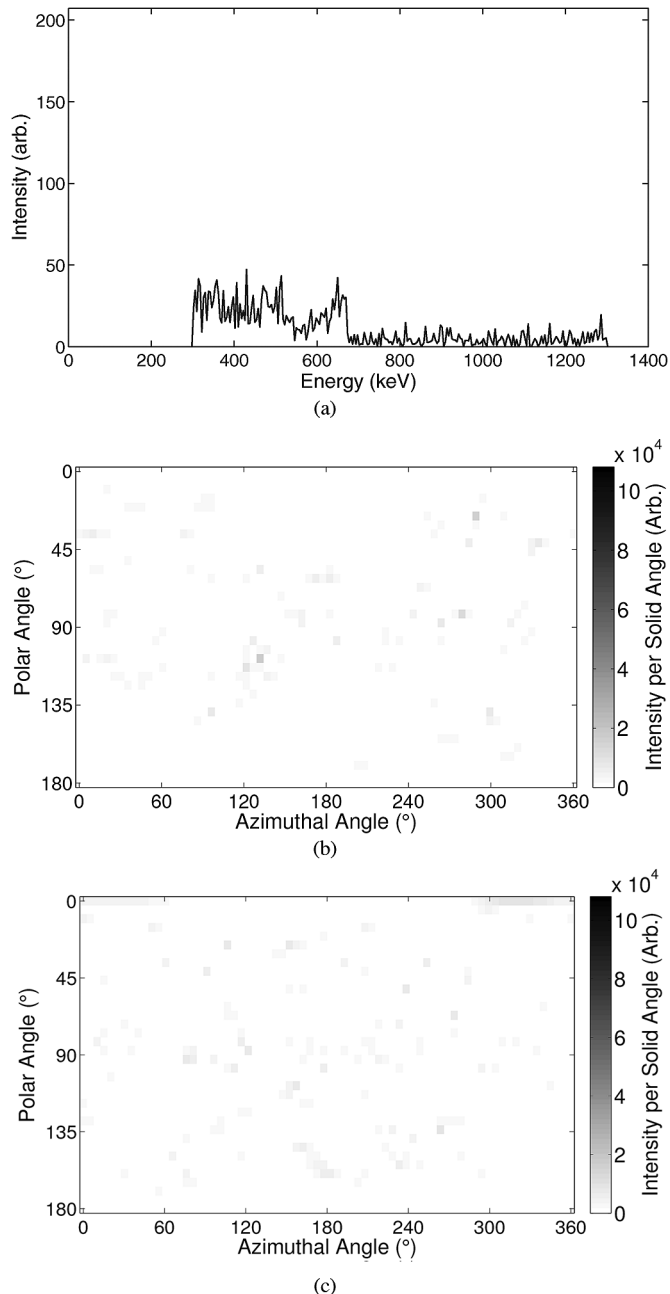
Fig. 10. Results for the backdrop space after 20 iterations of the proposed motion-compensated EM algorithm for a ^{137}Cs source moving counterclockwise and a ^{22}Na source moving clockwise: (a) reconstructed incident energy spectrum for the entire backdrop space, (b) reconstructed spatial distribution for the ^{137}Cs energy window (620–700 keV), and (c) reconstructed spatial distribution for the ^{22}Na energy window (490–530 keV and 1100–1200 keV).

Fig. 11. Results for the two target-object spaces after 20 iterations of the proposed motion-compensated EM algorithm for a ^{137}Cs source moving counterclockwise and a ^{22}Na source moving clockwise: (a) reconstructed incident energy spectrum for both targets, (b) reconstructed spatial distribution for the ^{137}Cs energy window (620–700 keV) in target object 1, (c) reconstructed spatial distribution for the ^{22}Na energy window (490–530 keV and 1100–1200 keV) in target object 1, (d) reconstructed spatial distribution for the ^{137}Cs energy window in target object 2, and (e) reconstructed spatial distribution for the ^{22}Na energy window in target object 2.

The results for the proposed model-based algorithm after 20 EM iterations are shown in Figs. 10 and 11. The desired results for this reconstruction would be zero (or some small amount of background) in the backdrop space, and a single hotspot at the ^{137}Cs energy in the first target object (which tracked the ^{137}Cs source), and a single hotspot at the ^{22}Na energies for the second target object (which tracked the ^{22}Na source). The backdrop results seen in Fig. 10 roughly show the desired results. Some ^{137}Cs and ^{22}Na intensity is incorrectly estimated in the backdrop, but this contamination is small and distributed in all

directions. Fig. 11 shows the results for the two target objects. Here, it is obvious that the first target object has a single hotspot at 662 keV and a zero distribution at the ^{22}Na energy window. Also, the second target object has a hotspot at the ^{22}Na energies and a flat distribution at the ^{137}Cs energy as desired. Finally, the estimated incident spectra for the two target objects show well-deconvolved ^{137}Cs and ^{22}Na energy spectra.

VI. CONCLUSIONS

We presented a model-based reconstruction method that successfully separates moving source(s) with known motion from stationary sources with minimal crosstalk contamination between sources. This new approach is an extension of the standard MLEM reconstruction for the combined energy and spatial domain. Even in the case of target objects that overlap

in the course of their motion, the proposed approach can estimate the contribution from each target object. This enables simultaneous image reconstruction of gamma-ray emissions from a number of simultaneously moving target objects and a nonmoving backdrop as long as the motion paths are known. We have demonstrated this method by using several situations and data from an 18-detector position-sensitive CdZnTe array system. Furthermore, this algorithm can be implemented for other list-mode imaging systems or for other applications, such as source detection.

APPENDIX

DERIVATION OF TIME-DEPENDENT LIST-MODE LOG LIKELIHOOD

This derivation was modified from [25].

Assume that the detection system is set to record photon interaction events for a preset time. In this case, the number of counts the system records will be a Poisson random variable M. We also assume that the detector records the time t_m of the mth recorded event as well as a set of attributes $\boldsymbol{v}_m$ describing the event, including the number of interactions as well as the locations and energies of each interaction. The log likelihood associated with these observations is

$$L(\lambda) = \log \left(p\left(\boldsymbol{v}_1, t_1, \ldots, \boldsymbol{v}_n, t_n | D_1, \ldots, D_n, M = n; \lambda\right) \right.$$
$$\left. \cdot P[M = n, D_1, \ldots, D_n; \lambda] \right) \quad (15)$$

where n is the total number of events recorded in a particular scan, D_m denotes that the mth event is detected, and λ is the intensity distribution in space and energy from (8). This expression describes the log of the joint probability of recording the attributes since they were detected and that exactly n events were detected, multiplied by the probability that n events were detected. We define the following term, which describes the expected count rate as a function of time, to simplify future expressions

$$\lambda_s(t) = \iint_\Omega s(\vec{r}, E, t) \lambda(\vec{r}, E, t) d\vec{r} dE. \quad (16)$$

The last term in the log likelihood, which follows a Poisson distribution, describes the probability of recording exactly $M = n$ counts during the scan time. Thus

$$P[M = n, D_1, \ldots, D_n; \lambda] = \frac{e^{-\bar{M}_\lambda} (\bar{M}_\lambda)^n}{n!} \quad (17)$$

where $\bar{M}_\lambda$ is the expected number of recorded counts for source distribution λ. Since $\lambda_s(t)$ is the instantaneous expected count rate, the expected total number of photons recorded over the scan time τ_d is

$$\bar{M}_\lambda = \int_0^{\tau_d} \lambda_s(t) dt. \quad (18)$$

The first part of the list-mode log likelihood can be rewritten using the chain rule as

$$p(\boldsymbol{v}_1, t_1, \ldots, \boldsymbol{v}_n, t_n | D_1, \ldots, D_n, M = n; \lambda)$$
$$= p(\boldsymbol{v}_1, \ldots, \boldsymbol{v}_n | t_1, \ldots, t_n, D_1, \ldots, D_n, M = n; \lambda)$$
$$\cdot p(t_1, \ldots, t_n | D_1, \ldots, D_n, M = n; \lambda). \quad (19)$$

Note that the recorded time t_m of each event cannot be included in the attribute vector $\boldsymbol{v}_m$ because the times follow a specific order and, thus, cannot be considered independent parameters. However, we do make the usual assumption that, given the event times, the attribute vectors are conditionally independent of each other (meaning we ignore dead time and pileup). Thus, the first term on the right-hand side of (19) can be further simplified to

$$p(\boldsymbol{v}_1, \ldots, \boldsymbol{v}_n | t_1, \ldots, t_n, D_1, \ldots, D_n, M = n; \lambda)$$
$$= \prod_{m=1}^n p(\boldsymbol{v}_m | t_m, D_m; \lambda). \quad (20)$$

The second term in (19) describes the conditional distribution of the ordered arrival times. For a Poisson random process, Ross [26, p. 37, 53] shows that

$$p(t_1, \ldots, t_n, D_1, \ldots, D_n | M = n; \lambda)$$
$$= \begin{cases} n! \prod_{m=1}^n q(t_m; \lambda) & 0 < t_1 < \ldots < t_n < \tau_d \\ 0 & \text{otherwise} \end{cases} \quad (21)$$

where

$$q(t_m; \lambda) = \begin{cases} \dfrac{\lambda_s(t_m)}{\bar{M}_\lambda} & 0 < t_1 < \ldots < t_n < \tau_d \\ 0 & \text{otherwise.} \end{cases} \quad (22)$$

Substituting (17)–(22) into (15) yields the following simplified expression for the list-mode log-likelihood for time-varying sources:

$$L(\lambda) = \sum_{m=1}^n \log \left(p(\boldsymbol{v}_m | t_m, D_m; \lambda) \lambda_s(t_m) \right) - \bar{M}_\lambda. \quad (23)$$

To analyze $p(\boldsymbol{v}_m | t_m, D_m; \lambda)$, we use total probability

$$p(\boldsymbol{v} | t, D; \lambda) = \iint_\Omega p(\boldsymbol{v} | \vec{r}, E, t, D; \lambda) p(\vec{r}, E | t, D; \lambda) d\vec{r} dE. \quad (24)$$

The first term in the integral is simply

$$p(\boldsymbol{v} | \vec{r}, E, t, D; \lambda) = p(\boldsymbol{v} | \vec{r}, E, t, D) \quad (25)$$

which is the distribution of recorded attributes expected from a source at location $\vec{r}$ and energy E recorded at time t. It is independent of the overall intensity distribution and is a key term in the system model (see (2)).

The second term in the integral is the probability density function (pdf) for the emission of a photon at position $\vec{r}$ and energy E. This term is related to λ but is a bit more complicated as

a result of the conditioning on D, because the photon is only *recorded* if the photon is detected. Particularly, the conditional distribution of the origin of the incident photons is

$$\mathsf{p}(\vec{r}, E | t, D; \lambda) = \frac{\mathsf{P}[D | \vec{r}, E, t; \lambda] \mathsf{p}(\vec{r}, E | t; \lambda)}{\mathsf{P}[D | t; \lambda]}. \quad (26)$$

The first term in the numerator is simply the conditional sensitivity of the system at time t, which is independent of λ, and the second term in the numerator is the pdf of the source intensity distribution $\mathsf{p}_t(\vec{r}, E)$, and is directly proportional to $\lambda(\vec{r}, E, t)$ since the decay constant of the radioactive isotopes is assumed to be long compared to the measurement time. Finally, the denominator is the total probability of detection at time t, which is calculated by integrating the sensitivity multiplied by $\mathsf{p}_t(\vec{r}, E)$. Thus, (26) reduces to

$$\mathsf{p}(\vec{r}, E | t, D; \lambda) = \frac{s(\vec{r}, E, t) \mathsf{p}_t(\vec{r}, E)}{\iint_{\Omega} s(\vec{r}', E') \mathsf{p}_t(\vec{r}', E') \mathrm{d}\vec{r}' \mathrm{d}E'}$$
$$= \frac{s(\vec{r}, E, t) \lambda(\vec{r}, E, t)}{\lambda_s(t)}. \quad (27)$$

Substituting (25) and (27) into (24) yields

$$\mathsf{p}(\boldsymbol{v} | t, D; \lambda) = \frac{1}{\lambda_s(t)} \iint_{\Omega} \mathsf{p}(\boldsymbol{v} | \vec{r}, E, D) s(\vec{r}, E, t) \lambda(\vec{r}, E, t) \mathrm{d}\vec{r} \mathrm{d}E. \quad (28)$$

After substituting (28) into (23), the time-dependent log-likelihood expression is

$$\mathsf{L}(\lambda) = \sum_{m=1}^{n} \log \left(\iint_{\Omega} \mathsf{p}(\boldsymbol{v}_m | \vec{r}, E, t_m, D_m) s(\vec{r}, E, t_m) \right.$$
$$\left. \cdot \lambda(\vec{r}, E, t_m) \mathrm{d}\vec{r} \mathrm{d}E \right) - \bar{M}_\lambda \quad (29)$$

which simplifies to (9) using (2).

Acknowledgment

The authors would like to thank the ORION team especially W. Kaye, Y. Boucher, and F. Zhang for their work on the detector array used for the measurements in this paper. They would also like to thank J. Berry for his work on the detector array and assembly of the actuator-positioning system.

References

[1] D. L. Snyder, "Parameter estimation for dynamic studies in emission-tomography systems having list-mode data," *IEEE Trans. Nucl. Sci.*, vol. NS-31, no. 2, pp. 925–931, Apr. 1984.

[2] M. Menke, M. Atkins, and K. Buckley, "Compensation methods for head motion detected during PET imaging," *IEEE Trans. Nucl. Sci.*, vol. 43, no. 1, pp. 310–317, Feb. 1996.

[3] J. Qi and R. Huesman, "List mode reconstruction for PET with motion compensation: A simulation study," in *Proc. IEEE Int. Symp. Biomed. Imag.*, 2002, pp. 413–416.

[4] E. Asma, T. Nichols, J. Qi, and R. Leahy, "4D PET image reconstruction from list mode data," in *Proc. IEEE Nucl. Sci. Symp. Conf. Rec.*, 2000, vol. 2, pp. 15/57–15/65.

[5] A. J. Reader, F. C. Sureau, C. Comtat, R. Trbossen, and I. Buvat, "Joint estimation of dynamic PET images and temporal basis functions using fully 4D ML-EM," *Phys. Med. Biol.*, vol. 51, no. 21, pp. 5455–5474, 2006.

[6] X. Niu, Y. Yang, and M. Wernick, "4D reconstruction of cardiac images using temporal Fourier basis functions," in *Proc. 15th IEEE Int. Conf. Image Process.*, 2008, Oct. 2008, pp. 2944–2947.

[7] T. Nichols, J. Qi, E. Asma, and R. Leahy, "Spatiotemporal reconstruction of list-mode PET data," *IEEE Trans. Med. Imag.*, vol. 21, no. 4, pp. 396–404, Apr. 2002.

[8] D. Gao, Y. Yao, F. Pan, T. Yu, B. Yu, L. Guan, W. Dixon, B. Yanoff, T.-P. Tian, and N. Krahnstoever, "Computer vision aided target linked radiation imaging," in *Proc. IEEE Conf. Comput. Vis. Pattern Recogn.*, Jun. 2012, pp. 1162–1169.

[9] T. Aucott, F. Jensen, and M. Bahr, Machine vision radiation detection system ARI, 2009.

[10] D. S. Hochbaum, "The multi-sensor nuclear threat detection problem," in *Operations Research and Cyber-Infrastructure*, ser. Oper. Res./Comput. Sci. Interfaces Ser. New York, USA: Springer, 2009, vol. 47, pp. 389–399.

[11] D. Xu and Z. He, "Gamma-ray energy-imaging integrated spectral deconvolution," *Nucl. Instrum. Methods Phys. Res. A, Accel. Spectrom. Detect. Assoc. Equip.*, vol. 574, no. 1, pp. 98–109, Apr. 2007.

[12] C. Wahl and Z. He, "Gamma-ray point-source detection in unknown background using 3D-position-sensitive semiconductor detectors," *IEEE Trans. Nucl. Sci.*, vol. 58, no. 3, pp. 605–613, Jun. 2011.

[13] D. Xu, Z. He, and F. Zhang, "Detection of gamma ray polarization using a 3-D position-sensitive CdZnTe detector," *IEEE Trans. Nucl. Sci.*, vol. 52, no. 4, pp. 1160–1164, Aug. 2005.

[14] D. Xu and Z. He, "Filtered back-projection in 4π Compton imaging with a single 3D position sensitive CdZnTe detector," *IEEE Trans. Nucl. Sci.*, vol. 53, no. 5, pp. 2787–2796, Oct. 2006.

[15] F. Zhang, Z. He, and C. E. Seifert, "A prototype three-dimensional position sensitive CdZnTe detector array," *IEEE Trans. Nucl. Sci.*, vol. 54, no. 4, pp. 843–848, Aug. 2007.

[16] H. H. Barrett, T. White, and L. C. Parra, "List-mode likelihood," *J. Opt. Soc. Amer. A*, vol. 14, no. 11, pp. 2914–2923, Nov. 1997.

[17] L. Mihailescu, K. Vetter, and D. Chivers, "Standoff 3D gamma-ray imaging," *IEEE Trans. Nucl. Sci.*, vol. 56, no. 2, pp. 479–486, Apr. 2009.

[18] W. Wang, C. Wahl, J. Jaworski, and Z. He, "Maximum-likelihood deconvolution in the spatial and spatial-energy domain for events with any number of interactions," *IEEE Trans. Nucl. Sci.*, vol. 59, no. 2, pp. 469–478, Apr. 2012.

[19] L. C. Parra and H. H. Barrett, "List-mode likelihood: EM algorithm and image quality estimation demonstrated on 2-D PET," *IEEE Trans. Med. Imag.*, vol. 17, no. 2, pp. 228–235, Apr. 1998.

[20] Y. Censor, "Finite series-expansion reconstruction methods," *Proc. IEEE*, vol. 71, no. 3, pp. 409–419, Mar. 1983.

[21] H. N. Multhei, B. Schorr, and W. Tornig, "On properties of the iterative maximum likelihood reconstruction method," *Math. Meth. Appl. Sci.*, vol. 11, no. 3, pp. 331–342, 1989.

[22] Z. He, W. Li, G. Knoll, D. Wehe, J. Berry, and C. Stahle, "3-D position sensitive CdZnTe gamma-ray spectrometers," *Nucl. Instrum. Methods Phys. Res. A, Accel. Spectrom. Detect. Assoc. Equip.*, vol. 422, pp. 173–78, 1999.

[23] F. Zhang, Z. He, G. Knoll, D. Wehe, and J. Berry, "3-D position sensitive CdZnTe spectrometer performance using third generation VAS/TAT readout electronics," *IEEE Trans. Nucl. Sci.*, vol. 52, no. 5, pp. 2009–2016, Oct. 2005.

[24] D. Xu, "Gamma-ray imaging and polarization measure using 3-D position-sensitive CdZnTe detectors," Ph.D. dissertation, Dept. Nucl. Eng. Radiol. Sci., Univ. Michigan, Ann Arbor, MI, USA, 2006.

[25] J. Fessler, *Image Reconstruction: Algorithms and Analysis* 2009, draft of book in preparation.

[26] S. M. Ross, *Stochastic Processes*. New York: Wiley, 1983.